J Mater Sci (2008) 43:3992–4000
DOI 10.1007/s10853-007-2433-9

REES RAWLINGS FESTSCHRIFT

# Creep and creep fracture of commercial aluminium alloys

**B. Wilshire · P. J. Scharning**

Received: 19 June 2007 / Accepted: 18 December 2007 / Published online: 3 April 2008


**Abstract** Using standard power law equations, creep rate and creep life measurements at 373–463 K are analysed for a series of aluminium alloys, namely, 2419, 2124, 8090 and 7010. The seemingly complex behaviour patterns are easily rationalized through a modified power law expression, which incorporates the activation energy for lattice diffusion in the alloy matrices (145 kJ $mol^{-1}$) and the value of the ultimate tensile stress at the creep temperature. By considering the changes in microstructure and creep curve shape as the test duration and temperature increase, all results are then interpreted straightforwardly in terms of the processes shown to govern strain accumulation and damage evolution. Moreover, the data rationalization procedures are also included in new relationships which superimpose the property sets onto sigmoidal 'master curves', allowing accurate prediction of the 100,000 h creep-rupture strengths of 2124 by extrapolation of creep lives determined from tests having a maximum duration of only around 1000 h.

## Introduction

Under sustained tensile loads at temperatures above about half of the absolute melting point, on plotting the increase in creep strain ($\varepsilon$) with time ($t$), most metals and alloys display normal creep curves. Thus, following the initial strain on loading, the creep rate ($\dot{\varepsilon} = d\varepsilon/dt$) decreases continuously during the primary stage, reaching a minimum or secondary value ($\dot{\varepsilon}_m$) before the accelerating tertiary stage leads to failure after a time ($t_f$). Yet, despite the distinctive shape of these normal curves, most theoretical and practical studies have discussed creep and creep fracture behaviour by focusing on the $\dot{\varepsilon}_m$ and $t_f$ values.

The creep life increases as $\dot{\varepsilon}_m$ decreases when the applied stress ($\sigma$) and the test temperature ($T$) are reduced [1], demonstrating that creep failure is strain controlled. Since the early 1950s, it has then become common practice to analyse the observed behaviour patterns using power law equations of the form

$$M/t_f = \dot{\varepsilon}_m = A\sigma^n \exp(-Q_c/RT) \quad (1)$$

where $M = \dot{\varepsilon}_m \cdot t_f$ and $R = 8.314$ $Jmol^{-1}$ $K^{-1}$. Unfortunately, the product ($\dot{\varepsilon}_m \cdot t_f$), the parameter ($A$), the stress exponent ($n$) and the activation energy for creep ($Q_c$) are themselves functions of stress and temperature.

This problem of 'variable constants' has usually been addressed by assuming that different creep processes become dominant in different stress/temperature regimes, with the dominant mechanism often identified by comparing measured and theoretically predicted values of $n$ and $Q_c$. For instance, with pure polycrystalline metals, creep occurs by diffusion-controlled dislocation processes when $n > 4$ at high stresses, with a decrease towards $n \cong 1$ at low stresses widely attributed to a transition to diffusional creep mechanisms not involving dislocation movement. However, the dislocation models proposed to explain $n > 4$ behaviour are incompatible with the available experimental evidence [2], while debate has continued for several decades over the rate-controlling mechanism when $n \cong 1$ [3].

The situation becomes even more complex when considering creep data obtained for alloys strengthened by dispersions of fine precipitates or insoluble particles. With these alloys, particularly at high-stress levels, it is

B. Wilshire (✉) · P. J. Scharning
Materials Research Centre, School of Engineering, University of Wales Swansea, Singleton Park, Swansea SA2 8PP, UK
e-mail: b.wilshire@swansea.ac.uk

frequently found that $n \gg 4$, while $Q_c$ is generally reported to be far larger than the activation energy for lattice diffusion in the alloy matrices. No agreement has been reached over the concepts advanced to account for these anomalously large and variable values of $n$ and $Q_c$ [4]. Moreover, from a practical viewpoint, power law approaches do not allow prediction of the properties exhibited by creep-resistant alloys under the conditions encountered during service, so many tests lasting up to 100,000 h must be completed to determine the long-term design strengths [5].

In contrast to traditional data analysis methods, alternative procedures for rationalization of $\dot{\varepsilon}_m$ and $t_f$ measurements allow straightforward interpretation of all features of the power law behaviour patterns documented for pure copper, without invoking creep mechanism transitions [6]. Hence, to demonstrate that these approaches are also applicable to precipitation-hardened alloys, the present report considers results available for a series of commercial aluminium alloys, namely, 2419 and 2124 [7], 8090 [8] and 7010 [9]. In addition, attention is directed to new relationships for data rationalization [6, 10–12], which have been developed to permit accurate prediction of long-term design strengths by extrapolation of short-term property sets.

## Materials and test procedures

The four wrought aluminium alloys were supplied in the form of plates, which were solution treated, water quenched, cold stretched and then aged. Details of the processing schedules are given in Table 1.

### Nominal compositions

The nominal compositions (wt.%) of the four alloys were as follows.

(a) 2419 (Al–6.3Cu–0.3Mn–0.15Zr), with a low content of iron and silicon, i.e., a high purity version of 2219.
(b) 2124 (Al–4.4Cu–1.5Mg–0.6Mn), again with low iron and silicon contents, i.e., a high purity version of 2024.
(c) 8090 (Al–1.3Cu–1.0Mg–0.1Zr–2.4Li), formulated to achieve a specific gravity of 2.53 Mg $m^{-3}$ as opposed to around 2.8 Mg $m^{-3}$ for conventional alloys.
(d) 7010 (Al–6.0Zn–2.4Mg–1.7Cu–0.13Zr), a composition similar to that of the more widely used alloy, 7075.

### Alloy microstructures

The microstructures in the as-received condition were revealed by optical and transmission electron microscopy [7–9].

(a) 2419 had an average grain diameter of about 0.12 mm, with some large copper-rich particles, which remained undissolved during solution treatment. The heat treatment produced a fine dispersion of plate-like $\theta'$ precipitates ($CuAl_2$), as shown in Fig. 1a.
(b) 2124 had an average grain diameter of around 0.15 mm, with some large particles of MnAl and a number of smaller $MnAl_6$ particles. A fine distribution of lath-like S precipitates was observed throughout the grains, with narrow precipitate-free zones (PFZs) at grain boundaries (<100 nm wide), as evident from Fig. 1b.
(c) 8090 had an elongated grain structure, with grain lengths up to 0.5 mm and widths of ~0.02 mm. Spherical $\delta'$ ($Al_3Li$) precipitates of 25 ± 10 μm diameter were distributed uniformly throughout the grains, with average PFZ widths of about 130 nm (Fig. 1c).
(d) 7010 also had an elongated grain structure, with grain lengths up to 0.5 mm and widths of ~0.05 mm. With this alloy, a dispersion of $ZrAl_2$ particles restricts extensive grain growth during heat treatment. GP zones as well as $\eta'$ and $\eta$ precipitates were present throughout the grains, with PFZ widths of around 70 nm (Fig. 1d).

### Creep testing procedures

For all four alloys, tensile creep tests were carried out using high-precision constant-stress machines described elsewhere [13].

**Table 1** Processing schedules for alloy manufacture

| Alloy | Plate thickness (mm) | Solution treatment (K) | Cold stretch (%) | Ageing temperature (K) | Ageing time (h) |
|---|---|---|---|---|---|
| 2419–T851 | 38 | 808 ± 4 | 1.5–3.0 | 450 | 18 |
| 2124–T851 | 63 | 768 ± 3 | 1.5 | 463 | >12 |
| 8090–T8771 | 37.5 | 819 ± 4 | 6.0 | 443 | 32 |
| 7010–T7351 | 25 | 745 ± 3 | 2.5–3.0 | 457 | 17 |

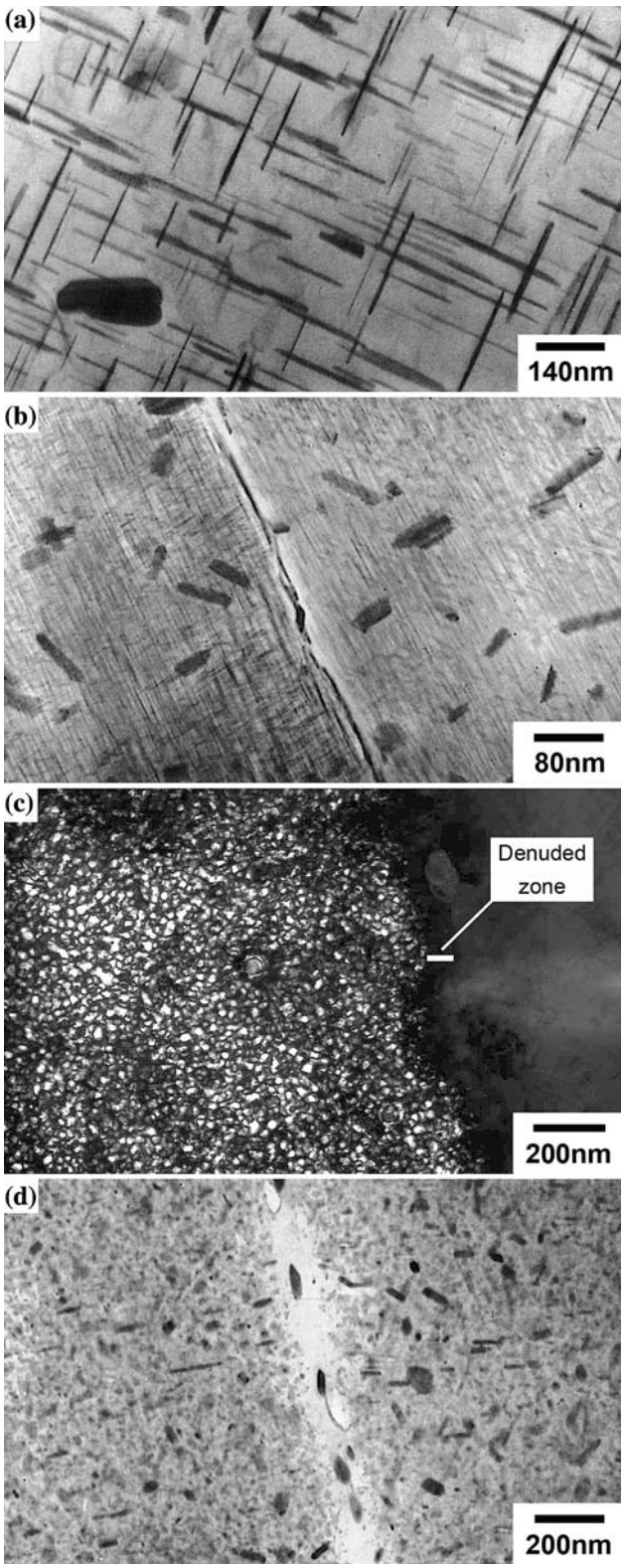


**Fig. 1** Transmission electron micrographs of (**a**) 2419, (**b**) 2124, (**c**) 8090 and (**d**) 7010 in the as-heat-treated condition

(a) Cylindrical specimens, having gauge lengths of 25.4 mm and diameters of 4 mm (with 9.5 mm threaded ends), were machined from the as-received plate samples.
(b) The creep tests were performed at 373, 409, 427, 445 and 463 K.
(c) At each temperature, the chosen stress range gave creep lives up to a maximum of around $10^7$ s (over 3 months).
(d) Although complete creep strain/time curves were recorded for each test, only the $\dot{\varepsilon}_m$ and $t_f$ values are now considered, together with the general variations in the curve shapes as the test conditions are altered. However, the detailed curve shape changes have been analysed previously [7–9] using the $\theta$ methodology [13].

## Results and discussion

Adopting Eq. 1, the variations of $\dot{\varepsilon}_m$ and $t_f$ with stress and temperature are illustrated for 8090 in Figs. 2 and 3, respectively. Representing the $\dot{\varepsilon}_m$ and $t_f$ measurements by sets of straight lines, on raising the test temperature from 373 to 463 K, the $n$ value decreased

(a) from ~41 to 16 with 2419,
(b) from ~28 to 6 with 2124,
(c) from ~32 to 5 with 8090 and
(d) from ~23 to 5 with 7010.

These $n$ value changes were accompanied by increases from $Q_c \cong 140$ kJ mol$^{-1}$ towards $Q_c \cong 230$ kJ mol$^{-1}$

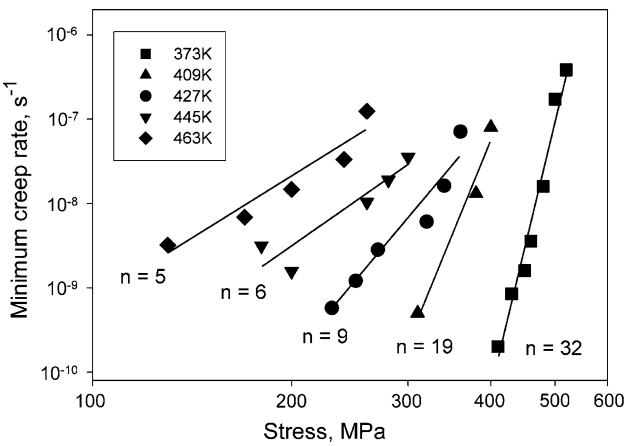


**Fig. 2** Stress dependence of the minimum creep rate at 373–463 K for 8090

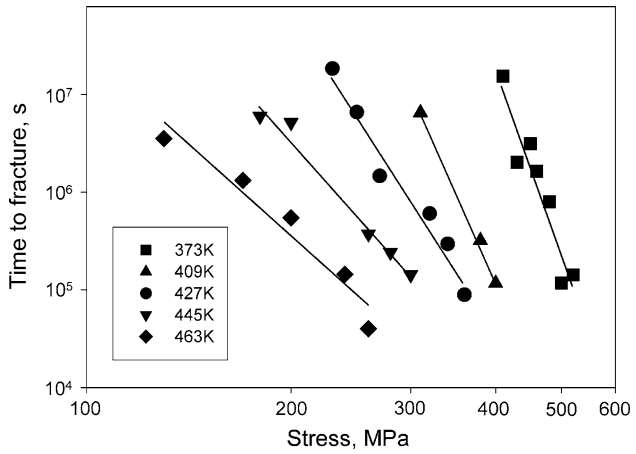


**Fig. 3** Stress dependence of the time to fracture at 373–463 K for 8090

with decreasing stress over the range of test conditions covered, i.e., results typical of the large $n$ and $Q_c$ values reported for particle-hardened alloys. Even so, the $\log \dot{\varepsilon}_m / \log \sigma$ and $\log t_f / \log \sigma$ plots at different temperatures are easily superimposed by normalizing the applied stress through the measured values of either the 0.2 % proof stress ($\sigma_Y$) or the UTS ($\sigma_{TS}$) at the appropriate creep temperatures [6–12], as illustrated for 8090 in Figs. 4 and 5. However, $\sigma_{TS}$ is preferred to $\sigma_Y$ because the results in Figs. 6 and 7 make it clear that, for all four alloys, $\dot{\varepsilon}_m \to \infty$ and $t_f \to 0$ as $(\sigma/\sigma_{TS}) \to 1$. In contrast, this systematic property description would not be achieved on replacing $(\sigma/\sigma_{TS})$ by $(\sigma/\sigma_Y)$, because the $(\sigma_{TS}/\sigma_Y)$ ratio varies for different alloys. Hence, choosing $\sigma_{TS}$ rather than $\sigma_Y$, Eq. 1 becomes

$$M/t_f = \dot{\varepsilon}_m = A^*(\sigma/\sigma_{TS})^n \exp(-Q_c^*/RT) \quad (2)$$

where $A^* \neq A$ and $Q_c^* \neq Q_c$. The $Q_c^*$ values in Eq. 2 are then determined from the temperature dependences of $\dot{\varepsilon}_m$ and $t_f$ at constant $(\sigma/\sigma_{TS})$, whereas $Q_c$ is calculated at constant $\sigma$ with Eq. 1. As evident from the rationalized curves presented in Figs. 4–7, $Q_c^* = 145$ kJ mol$^{-1}$, a value close to that for lattice diffusion in the aluminium alloy matrices.

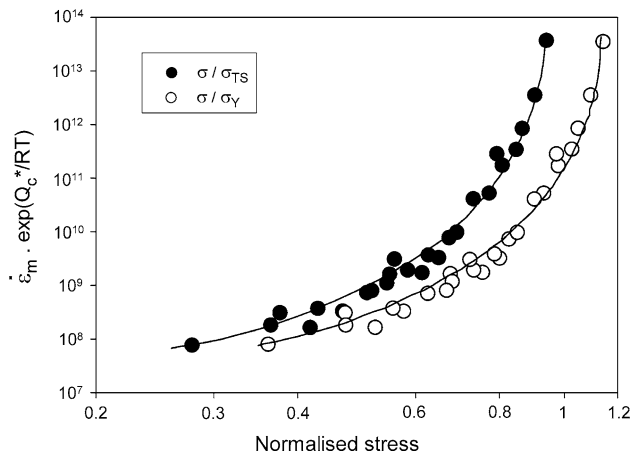


**Fig. 4** The power law dependences of the temperature-compensated creep rate on $(\sigma/\sigma_Y)$ and $(\sigma/\sigma_{TS})$ for 8090, with $Q_c^* = 145$ kJ mol$^{-1}$

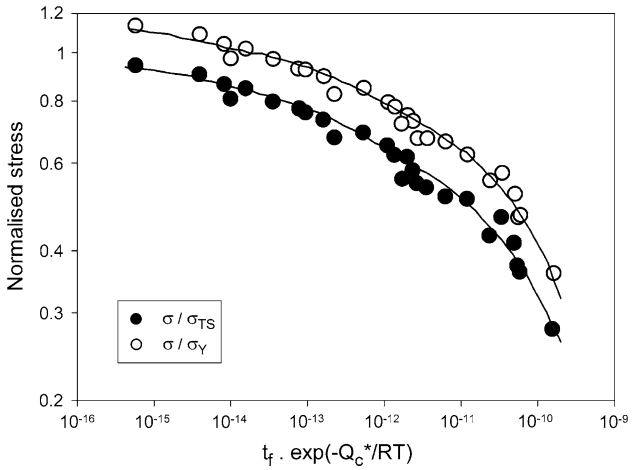


**Fig. 5** The power law dependences of the temperature-compensated creep life on $(\sigma/\sigma_Y)$ and $(\sigma/\sigma_{TS})$ for 8090, with $Q_c^* = 145$ kJ mol$^{-1}$

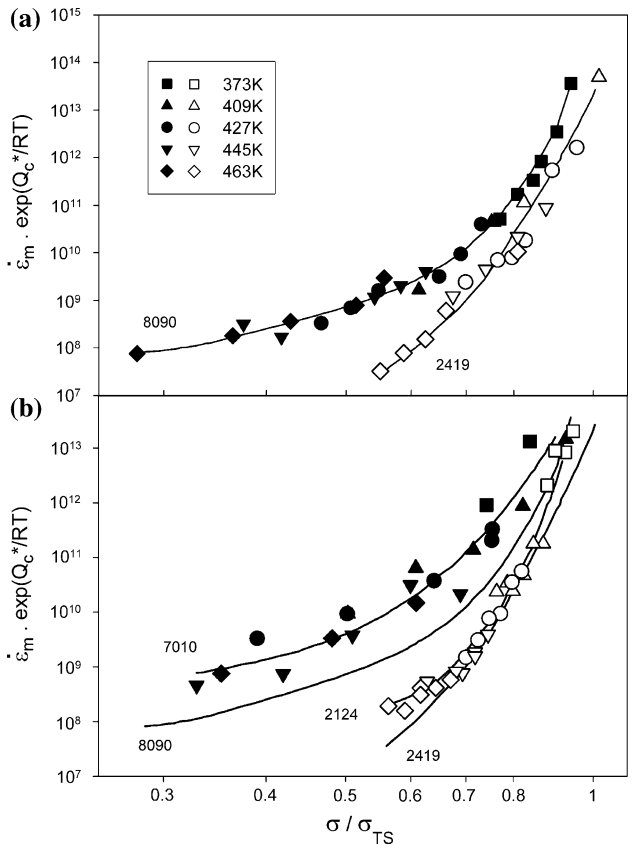


**Fig. 6** The dependences of the temperature-compensated creep rate on $(\sigma/\sigma_{TS})$ for 2419, 2124, 8090 and 7010, using Eq. 2 with $Q_c^* = 145$ kJ mol$^{-1}$

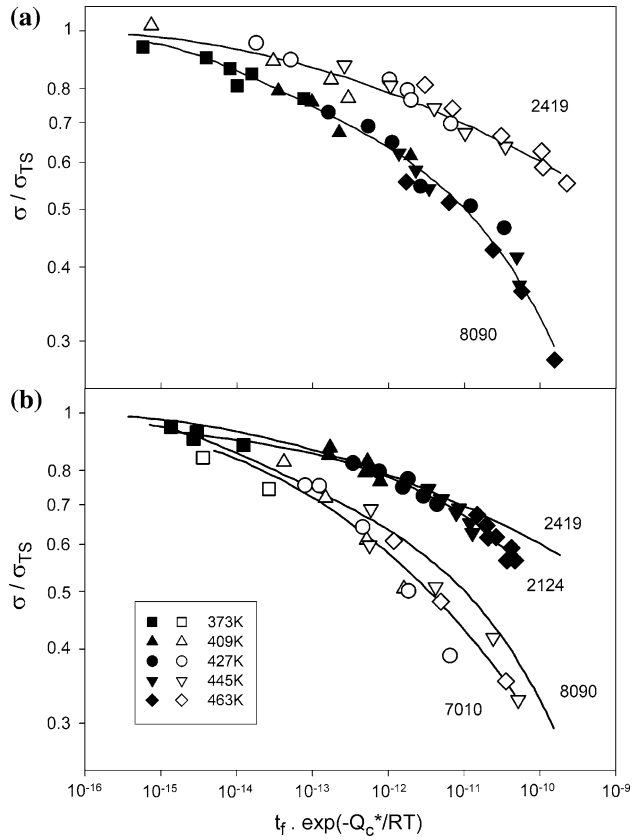


**Fig. 7** The dependences of the temperature-compensated creep life on $(\sigma/\sigma_{TS})$ for 2419, 2124, 8090 and 7010, using Eq. 2 with $Q_c^* = 145$ kJ mol$^{-1}$

Equation 2 avoids the large and variable $Q_c$ values observed with Eq. 1, but does not eliminate the decrease from $n > 20$ towards $n \cong 5$, a trend expected to continue towards $n \cong 1$ as the stress is lowered (Figs. 4–7). One early attempt to explain the anomalously large $n$ values then suggested [14] that creep occurs not under the full applied stress ($\sigma$) but under a reduced stress ($\sigma$–$\sigma_o$), such that

$$\dot{\varepsilon}_m \propto (\sigma - \sigma_o)^m \quad (3)$$

where $m = 4$, with $\sigma_o$ now called a 'threshold stress'. Comparing Eqs. 1 and 3, $n \cong m \cong 4$ when $\sigma_o \cong 0$ or when $\sigma_o \propto \sigma$, whereas $n > m$ when $\sigma_o$ is large. This approach has been widely applied to creep of particle-hardened alloys, but little progress has been made because $\sigma_o$ cannot be measured or predicted reliably [4].

Although the rationalized data sets in Figs. 6 and 7 suggest that $n$ decreases continuously as $(\sigma/\sigma_{TS})$ decreases, such curves could also be represented by a series of straight-line segments drawn to show gradients of $n > 4$, $n \cong 4$ and $n \cong 1$, with different creep mechanisms assumed to be dominant as $n$ changes. For this reason, it is necessary to clarify the processes governing creep and creep fracture of the four aluminium alloys.

## Creep deformation and damage processes

Normal creep curves are generally taken to show that distinct primary, secondary and tertiary stages occur prior to failure. Over the last 50 years or so, most theoretical studies have then sought to explain phenomena such as the variations of $n$ and $Q_c$ in Eq. 1 (Figs. 2 and 3) by proposing mechanisms to account for secondary or 'steady state' behaviour. However, much information is lost by ignoring the primary and tertiary components. First, the overall curve shape can vary dramatically as the test conditions are altered, as illustrated by the change from a primary-dominated to a tertiary-dominated shape as the test duration and temperature increase with 8090 (Fig. 8). Second, replotting $\varepsilon/t$ curves to display the variations in creep strain rate ($\dot{\varepsilon}$) with time ($t$) demonstrates that a minimum rate ($\dot{\varepsilon}_m$) rather than a 'steady state' value is reached when the decaying primary rate is offset by the tertiary acceleration (Fig. 9). Moreover, when this pattern of shape change is recorded, by measuring the time to the minimum rate ($t_m$), a decrease from $(t_m/t_f) > 0.5$ towards $(t_m/t_f) < 0.1$ occurs as the stress is reduced and the temperature is raised (Figs. 8 and 9). On this basis, instead of considering 'steady state' creep mechanisms, standard data sets should be interpreted in terms of the processes controlling creep strain accumulation and the damage phenomena causing the tertiary acceleration and eventual fracture.

Over the stress–temperature ranges covered in Figs. 4–7, with $n > 4$, creep occurs by diffusion-controlled dislocation movement in the alloy matrices, in line with the fact that $Q_c^* = 145$ kJ mol$^{-1}$. The primary creep rate then decays with time because dislocation movement becomes more difficult as the dislocation density increases with increasing creep strain. In contrast, several different

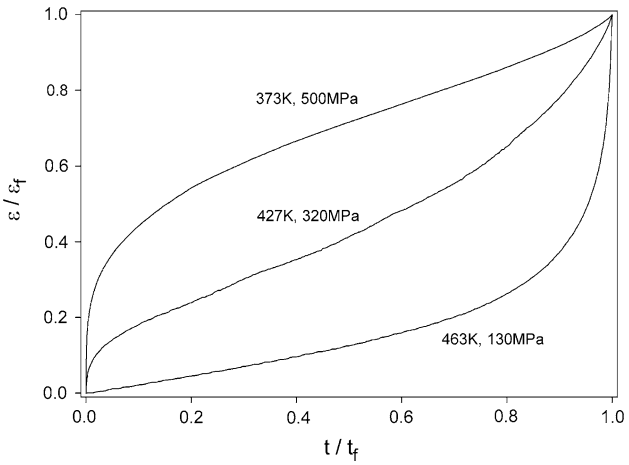


**Fig. 8** Variations in the shape of the normal creep strain/time curves, plotted to show normalized creep strain $(\varepsilon/\varepsilon_f)$ against normalized time $(t/t_f)$ as the stress–temperature conditions are changed for 8090, where $\varepsilon_f$ is the total creep strain to failure

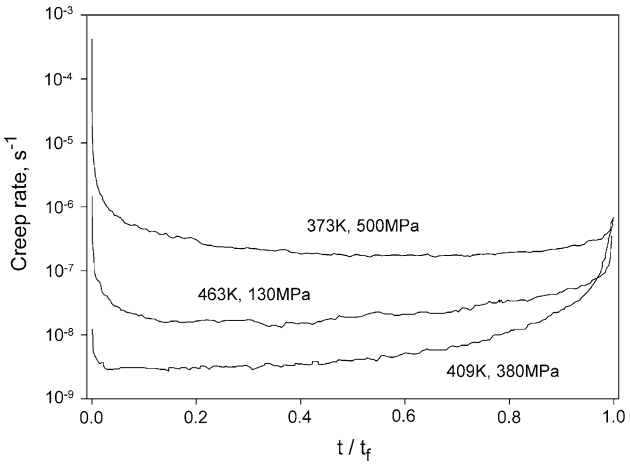


**Fig. 9** The creep strain/time curves for 8090 from Fig. 8 replotted to show the variations in creep strain rate with normalized time ($t/t_f$)

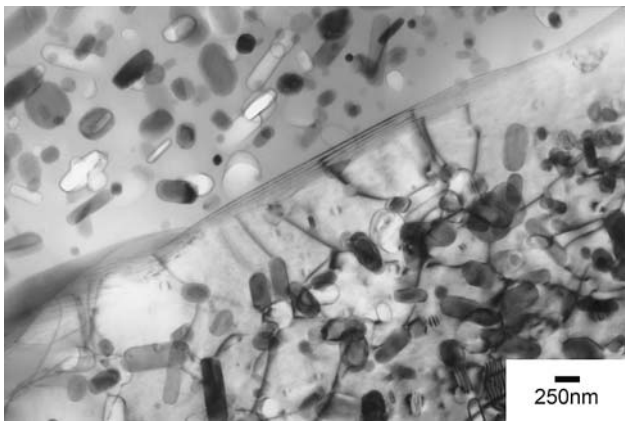


**Fig. 10** Transmission electron micrograph showing the precipitate distribution present in 7010 after 1915 ks (532 h) under a stress of 75 MPa at 473 K

damage processes can start the tertiary acceleration, while more than one process can contribute to the subsequent rate of acceleration. The phenomena responsible for initiating the tertiary stage and causing eventual failure can also differ. Even so, the systematic variations in creep curve shape and the microstructural changes occurring with the four aluminium alloys can clarify the relative importance of the different damage processes as the test conditions are modified [7–9].

(a) With 2419, limited tertiary stages were found at temperatures up to 445 K, whereas a gradual change from primary-dominated to tertiary-dominated curve shapes was recorded for the other alloys as the test duration and test temperature increased, as illustrated for 8090 in Figs. 8 and 9. This pattern of curve shape variation was increasingly obvious in the order 2419, 2124, 8090 and 7010.

(b) The extent to which microstructural instability was apparent also increased in the order 2419, 2124, 8090 and 7010. While little evidence was found for 2419, significant coarsening of precipitates was accompanied by increases in the PFZ widths with the other alloys. For example, with 7010, GP zones were not detected after creep exposure at 409 K and above, while the $\eta'$ and $\eta$ precipitates coarsened appreciably. In addition, the PFZ width increased from ~70 nm to around 0.1 to 0.3 μm after creep at 473 K (Fig. 10).

(c) Fracture of 2419 and 2124, produced with equiaxed grain structures, was caused by intergranular cavitation without significant neck formation. In contrast, with the tensile stresses applied parallel to the elongated grain axes, 8090 and 7010 failed in a transgranular manner when the extent of necking increased as the stress was reduced at 409 K and above.

(d) This evidence reveals that the tertiary acceleration is a consequence of cavitation with 2419 and also with 2124 at 423 K and below. With 2124 at higher temperatures and with 8090 and 7010 at 409 K and above, tertiary creep starts because of the loss of creep strength associated with microstructural instability, even though the processes causing failure differed. These observations are then fully consistent with the patterns of curve shape change [7–9].

## Formation of precipitate-free zones

There is general agreement that creep occurs by diffusion-controlled dislocation processes when $n > 4$. However, it is widely believed that diffusional creep mechanisms govern strain accumulation when $n \to 1$ as the applied stress is reduced. In this context, the formation of particle-free zones (PFZs) at grain boundaries has often been quoted as providing definitive evidence for the dominant role of diffusional creep under low-stress conditions with precipitation-hardened alloys [15–17]. Yet, the electron micrographs presented in Fig. 1 demonstrate that PFZs can be present even in the as-received alloys, with the PFZ widths increasing progressively as the test duration and temperature increase, as illustrated for 7010 in Fig. 10. Moreover, with 2124 [7], 8090 [8] and 7010 [9], the PFZs develop under stress–temperature combinations such that $n > 4$, so that dislocation processes determine the creep behaviour. In fact, it is apparent from Fig. 10 that the PFZs provide locations for easy dislocation movement in the low stress regime. Hence, the formation and growth of PFZs do not offer valid support for the view that a transition from dislocation to diffusional creep mechanisms accounts for the decrease from $n > 4$ towards $n \cong 1$ at low stresses.

A new approach to creep data analysis

In line with the extent to which microstructural instability causes the change from primary-dominated to tertiary-dominated curve shapes, the curvatures of the $\log[\dot{\varepsilon}_m \cdot \exp(Q_c^*/RT)]/\log(\sigma/\sigma_{TS})$ and $\log[t_f \cdot \exp(-Q_c^*/RT)]/\log(\sigma/\sigma_{TS})$ relationships in Figs. 6 and 7 increase in the order 2419, 2124, 8090 and 7010. With the microstructural changes and curve shape variations closely linked, the gradual fall in $n$ value as $(\sigma/\sigma_{TS})$ decreases then appears to be attributable not to creep mechanism transitions but to the complex dependence of $\dot{\varepsilon}_m$ (and therefore $t_f$) on the systematic changes in creep curve shape as the test conditions are altered [13]. In addition, because $n$ decreases in an unpredictable manner as $(\sigma/\sigma_{TS})$ falls (Figs. 6 and 7), even Eq. 2 fails to allow reliable estimation of long-term performance by extrapolation of short-term measurements. Hence, new relationships have been introduced for analysis of creep and creep fracture properties [6, 10, 11], building on the data rationalization achieved by normalizing $\sigma$ through $\sigma_{TS}$ (Eq. 2).

The $\sigma_{TS}$ value represents the maximum stress which can be applied at the creep temperature, so data sets can be considered over the complete stress range from $(\sigma/\sigma_{TS}) = 1$ to $(\sigma/\sigma_{TS}) = 0$. Valid relationships devised to quantify creep and creep-rupture measurements must then make it evident not only that $\dot{\varepsilon}_m \rightarrow \infty$ and $t_f \rightarrow 0$ as $(\sigma/\sigma_{TS}) \rightarrow 1$, but also that $\dot{\varepsilon}_m \rightarrow 0$ and $t_f \rightarrow \infty$ as $(\sigma/\sigma_{TS}) \rightarrow 0$. These essential requirements are met by replacing Eq. 2, so that the stress and temperature dependences of the creep lives are described as [6, 10–12]

$$(\sigma/\sigma_{TS}) = \exp\{-k_1[t_f \cdot \exp(-Q_c^*/RT)]^u\} \quad (4)$$

with a comparable expression

$$(\sigma/\sigma_{TS}) = \exp\{-k_2[\dot{\varepsilon}_m \cdot \exp(Q_c^*/RT)]^v\} \quad (5)$$

quantifying the $\dot{\varepsilon}_m$ values. The straightforward way in which these new relationships allow data rationalization and interpretation is now demonstrated by using Eqs. 4 and 5 to re-analyze the $\dot{\varepsilon}_m$ and $t_f$ measurements for 8090 (Figs. 2–5).

The values of $k_1$ and $u$ in Eq. 4 are determined by plotting $\ln[t_f \cdot \exp(-145{,}000/RT)]$ as a function of $\ln[-\ln(\sigma/\sigma_{TS})]$, with a least-squares analysis giving $k_1 = 176.8$ and $u = 0.22$ for 8090 (Fig. 11). With Eq. 5, equivalent procedures give $k_2 = 63.8$ and $v = -0.22$ (Fig. 12), although the precision with which the coefficients can be quantified is influenced by data scatter. Inserting these values into Eqs. 4 and 5 then produces the sigmoidal 'master curves' for 8090 shown in Figs. 13 and 14. However, no long-term data was found for 8090, so the accuracy of the predictions made over extended stress–temperature ranges in Figs. 13 and 14 could not be

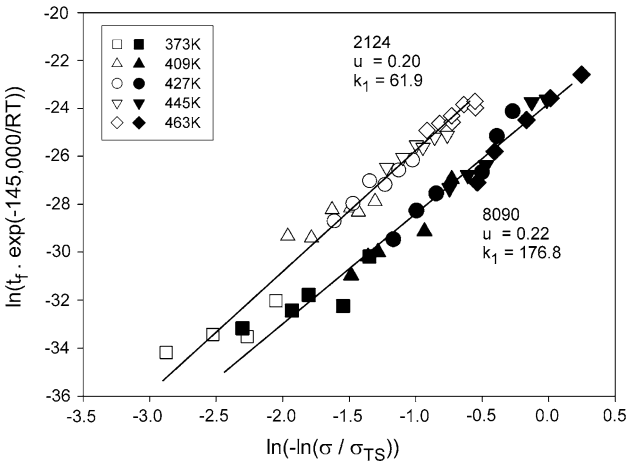


**Fig. 11** Plots of $\ln[t_f \cdot \exp(-145{,}000/RT)]$ against $\ln[-\ln(\sigma/\sigma_{TS})]$ for short-term tests, giving $k_1 = 176.8$ and $u = 0.22$ for 8090 (*full symbols*) and $k_1 = 61.9$ and $u = 0.20$ for 2124 (*open symbols*) in Eq. 4

assessed objectively. For this reason, Eqs. 4 and 5 were also adopted to analyse the short-term $\dot{\varepsilon}_m$ and $t_f$ measurements for 2124 (Figs. 11–14), the only one of the present alloys for which long-term stress-rupture properties have been determined [5]. Clearly, the data trends for 2124 and 8090 are similar. Several features of the results achieved then merit comment.

(a) For 2124, the short-term creep lives are included in Fig. 11, giving $k_1 = 61.9$ and $u = 0.20$. Incorporating these values into Eq. 4 produces the sigmoidal 'master curve' in Fig. 15, accurately predicting the independently determined data for stress ranges causing failure in times up to 100,000 h at 373–473 K [5].

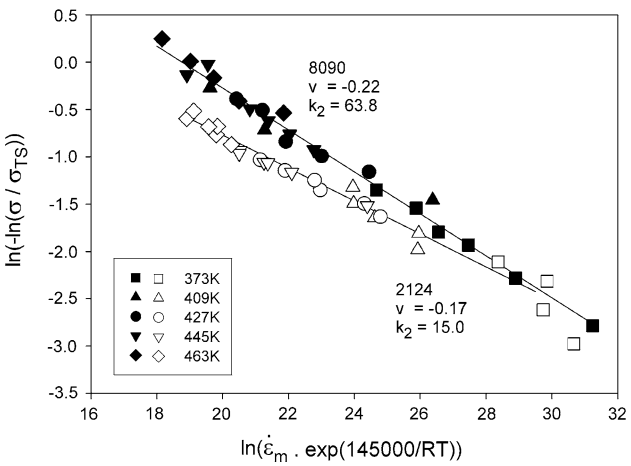


**Fig. 12** The variation of $\ln[\dot{\varepsilon}_m \cdot \exp(-145{,}000/RT)]$ with $\ln[-\ln(\sigma/\sigma_{TS})]$ for short-term tests, giving $k_2 = 63.8$ and $v = -0.22$ for 8090 (*closed symbols*) and $k_2 = 15.0$ and $v = -0.17$ for 2124 (*open symbols*) in Eq. 5

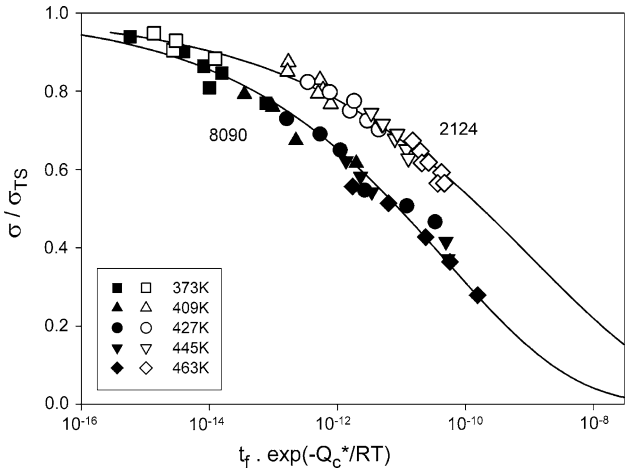


**Fig. 13** The sigmoidal variations of the temperature-compensated creep life with ($\sigma/\sigma_{TS}$) for 8090 (*full symbols*) and 2124 (*open symbols*), using Eq. 4 with $Q_c^* = 145$ kJ mol$^{-1}$. The behaviour shown over extended stress–temperature ranges (*solid lines*) were predicted using Eq. 4 by incorporating the $k_1$ and $u$ values derived in Fig. 11 from short-term creep life measurements

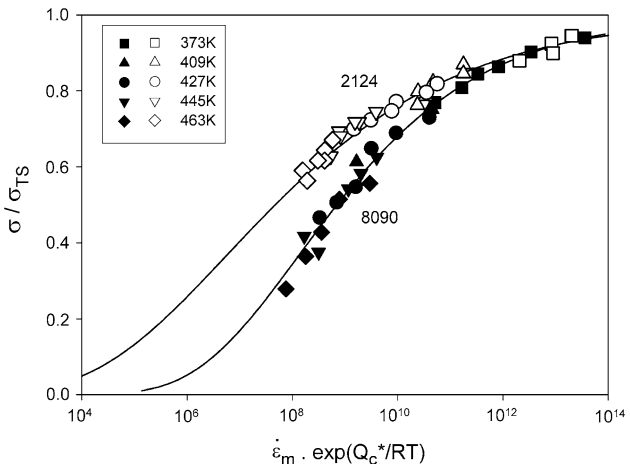


**Fig. 14** The sigmoidal variations of the temperature-compensated minimum creep rate with ($\sigma/\sigma_{TS}$) for 8090 (*full symbols*) and 2124 (*open symbols*), using Eq. 5 with $Q_c^* = 145$ kJ mol$^{-1}$. The behaviour shown over extended stress–temperature ranges (*solid lines*) was predicted using Eq. 5 by incorporating the $k_2$ and $v$ values derived in Fig. 12 from short-term creep rate measurements

(b) Adopting standard power law approaches, decreases from $n > 4$ towards $n \cong 1$ are commonly linked to transitions from dislocation to diffusional creep mechanisms but, if different processes control the creep rates and creep lives in different stress–temperature regimes, analysing data from one mechanism regime would not predict behaviour in another regime. Using Eq. 4 (Fig. 15), the fact that $t_f$ values for 2124 from tests lasting up to only 1000 h (when $n > 4$) allow accurate prediction of long-term properties (when $n \rightarrow 1$) supports the view that variations in $n$ value are not attributable to transitions in the dominant 'steady state' creep mechanism [13].

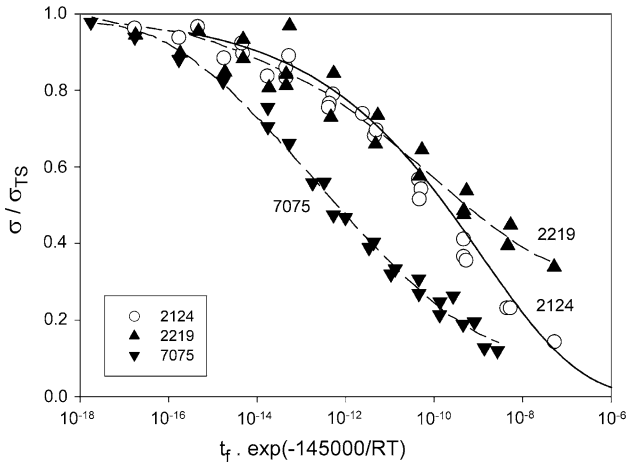


**Fig. 15** The sigmoidal variations of the temperature-compensated creep lives with ($\sigma/\sigma_{TS}$) predicted for 2124 by incorporating the $k_1$ and $u$ values derived in Fig. 11 from short-term creep life measurements (*solid line*). Clearly, these predictions accurately match the measured stress-rupture properties [5] determined for stress ranges giving creep lives up to 100,000 h at 373–473 K for 2124 (*open symbols*). Also included are the behaviour patterns obtained using Eq. 4 (with $Q_c^* = 145$ kJ mol$^{-1}$) to represent long-term data sets [5] for 2219 and 7075 (*broken lines*)

(c) Although long-term stress-rupture measurements were not found for 2419 and 7010, this information is available at 373–473 K [5] for 2219 (a less pure variant of 2419) and for 7075 (having a composition similar to 7010). Hence, adopting Eq. 4, these results are included in Fig. 15. In line with the extent to which the loss of creep resistance due to precipitate coarsening affects the behaviour patterns displayed by 2419, 2124, 8090 and 7010, the ($\sigma/\sigma_{TS}$) values which can be sustained without failure occurring in a stipulated time at the same creep temperature decreases in the order 2219, 2124 and 7075 (Fig. 15).

(d) As previously reported for a series of 9–12% chromium steels for power and petrochemical plant [11, 12], the results in Fig. 15 indicate that Eq. 4 allows accurate estimation of 100,000 h rupture strengths by extended extrapolation of short-term measurements. Validation of the new methodology by independent analysis of property sets for other creep-resistance alloys could then achieve a marked reduction in the times and costs of acquiring long-term engineering design data.

## Conclusions

For a series of commercial aluminium alloys, dislocation processes control creep strain accumulation, without a

transition to diffusional creep mechanisms occurring with decreasing applied stress. However, differences in the relative importance of the various damage processes governing the tertiary acceleration and failure determine the extent to which a gradual change from primary-dominated to tertiary-dominated creep curve shapes takes place as the test duration and temperature increase. The anomalous variations in $n$ and $Q_c$ value found using standard power law equations are then attributable not to transitions in the dominant creep mechanism but to the complex dependences of the creep rate and creep life on the systematic changes in creep curve shape as the test conditions are altered. Even so, the creep rates and creep lives recorded at different temperatures are effectively superimposed onto 'master curves' using a modified power-law expression which involves the appropriate UTS values and the activation energy for lattice diffusion in the alloy matrices (145 kJ $mol^{-1}$). Moreover, these data rationalization procedures are incorporated into new relationships, which allow extended extrapolation of short-term property sets. Although the predictive accuracy should improve as the extent of the projection is reduced, the independently determined 100,000 h creep-rupture strengths of alloy 2124 are estimated accurately by analysing creep life measurements from tests lasting up to only 1000 h. Hence, validation of this straightforward predictive methodology would minimize the scale and expense of the protracted experimental programmes currently undertaken to obtain long-term creep design data.

## References


1. Monkman FC, Grant NJ (1956) Proc ASTM 56:593
2. Nabarro FRN (2004) Mater Sci Eng A A387:659
3. Mishra RS, Mukherjee AK, Murty KL (eds) (1999) Creep behaviour of advanced materials for the 21st century. TMS, Warrendale, PA, p 391
4. Arzt E (1991) Res Mechanica 399:31
5. Kaufman JG (1999) Properties of aluminium alloys. ASM, Materials Park, OH
6. Wilshire B, Battenbough AJ (2007) Mater Sci Eng A A443:156
7. Burt H, Wilshire B (2004) Metall Mater Trans A 35A:1691
8. Burt H, Wilshire B (2005) Metall Mater Trans A 36A:1219
9. Burt H, Wilshire B (2006) Metall Mater Trans A 37A:1005
10. Wilshire B, Burt H, Lavery N (2006) Mater Sci Forum 519–521:1041
11. Wilshire B, Scharning PJ (2007) Scripta Mater 56:701
12. Wilshire B, Scharning PJ (2007) Scripta Mater 56:1023
13. Evans RW, Wilshire B (1985) In: Creep of metals and alloys. The Institute of Metals, London
14. Williams KR, Wilshire B (1973) Metal Sci J 7:176
15. Harris JE, Jones RB (1963) J Nucl Mater 10:360
16. Burton B, Reynolds GL (1995) Mater Sci Eng A A191:135
17. Srivastava V, Williams JP, McNee KR, Greenwood GN, Jones H (2004) Mater Sci Eng A A382:50